https://doi.org/10.5194/egusphere-2026-3211
Preprint. Discussion started: 5 August 2026

Nonlinear and regime-dependent precursor effects shape wintertime $PM_{2.5}$ formation in Beijing under calm conditions

Honglin Li[1], Xinwen Liu[2], and Song Xi Chen[3]

[1]School of Mathematical Sciences, Peking University, Beijing, China
[2]Yunnan Key Laboratory of Statistical Modeling and Data Analysis, Yunnan University, Kunming 650500, China
[3]Department of Statistics and Data Science, Tsinghua University, Beijing, China

Correspondence: Song Xi Chen (sxchen@tsinghua.edu.cn)

Abstract.

Wintertime $PM_{2.5}$ pollution in Beijing is increasingly governed by secondary aerosol formation, with sulfate and nitrate constituting the dominant inorganic components. However, quantifying the contribution of ambient SO_2 and NO_2 to $PM_{2.5}$ formation from observational data remains challenging because precursor–$PM_{2.5}$ relationships are confounded by meteorological variability, regional transport, and unmeasured emissions. Using routine monitoring data from Beijing heating seasons during 2016–2023, we develop an episode-based causal framework that restricts the analysis to calm periods to address transport-related confounding, and estimates nonlinear precursor responses using shape-constrained additive models incorporating emission proxies and precursor effect modification.

The proxy-calibrated model shows that combustion-related primary emissions remain the dominant unresolved confounder during calm episodes. Precursor concentrations lagged by 2–3 h explain short-term $PM_{2.5}$ changes, with faster apparent secondary processing in the pollution-hotspot southeastern urban area. Effect-modification analysis indicates that the SO_2 response is primarily regulated by thermal conditions. Annual attribution shows that SO_2 reductions dominated precursor-associated $PM_{2.5}$ improvements in the early years, but their contribution weakened as ambient SO_2 declined and its marginal effect diminished at low concentrations. In contrast, NO_2 sensitivity increases consistently at higher O_3 levels, suggesting that elevated O_3 in recent years may have enhanced nitrate-related $PM_{2.5}$ formation, consistent with the increased benefits associated with NO_2 reductions after 2020. These results indicate a transition toward increasingly nitrate-sensitive wintertime $PM_{2.5}$ formation in Beijing and show that routine monitoring data can provide chemically interpretable precursor sensitivities when transport and emission confounding are explicitly constrained.

1 Introduction

Ambient fine particulate matter ($PM_{2.5}$) pollution remains a leading global environmental risk factor, contributing to millions of premature deaths annually from cardiovascular and respiratory diseases (World Health Organization, 2021). While the World Health Organization (WHO) has progressively tightened its air quality guideline (AQG) level for annual $PM_{2.5}$ from 10 to 5 μg m^{-3}, recent global and regional assessments indicate that only a small fraction of the world's population resides in areas meeting this standard (Yu et al., 2023; Gouveia et al., 2021; Han et al., 2022). For regions still exceeding the WHO Interim

https://doi.org/10.5194/egusphere-2026-3211
Preprint. Discussion started: 5 August 2026

Target-1 (35 μg m^{-3}), the revised health-based thresholds imply an increasingly wide gap between current air quality and levels required for adequate health protection (Ouyang et al., 2022; Ma et al., 2025).

Developing economies such as China have achieved remarkable progress through stringent policies, but the recent slowing pace of improvement suggests diminishing marginal returns to conventional control measures (Chen Group, 2025); Beijing exemplifies this challenge, as despite phasing out coal combustion its wintertime $PM_{2.5}$ levels persistently remain above the WHO air quality guideline, necessitating a shift toward precision-oriented strategies. Secondary formation is a dominant driver of wintertime $PM_{2.5}$ in northern China (Ma et al., 2017; Xu et al., 2019; Sun et al., 2021), and regulating precursors such as SO_2 and NO_2 is central to air quality policy. However, quantifying their causal and marginal effects on $PM_{2.5}$ from observational data remains difficult, because meteorology, regional transport, and emission variability are tightly intertwined. Capturing the regime-dependent behavior of these precursors is therefore critical for designing cost-effective control strategies in a changing atmosphere.

Existing approaches have provided important insights into secondary $PM_{2.5}$ formation from complementary perspectives, but robust empirical evidence on precursor–$PM_{2.5}$ response mechanisms under ambient conditions remains limited. Process-based chemical transport models (e.g., CMAQ, CAMx, WRF-Chem) enable controlled scenario analysis and have been widely used to investigate atmospheric processes, but their results remain sensitive to uncertainties in chemical mechanisms, emission inventories, and poorly constrained secondary pathways (Kitayama et al., 2019; Luecken et al., 2019; Zhang et al., 2019). Receptor-based methods such as Positive Matrix Factorization (PMF) can quantify secondary components from particle composition but cannot directly attribute them to ambient precursor concentrations or disentangle local formation from regional transport (Kong et al., 2020; Yang et al., 2018). Although isotope tracer techniques can help quantify oxidation pathways and source contributions (Guo et al., 2016), they require extensive sampling and may be limited by discrepancies between laboratory-derived parameters and those under real atmospheric conditions.

In this context, statistical causal inference offers a complementary, data-driven framework that leverages long-term observational data while allowing the incorporation of basic physicochemical constraints. This approach avoids reliance on the highly specific mechanistic assumptions embedded in detailed equations and empirical parameters (Liang et al., 2015; Chen et al., 2019; Zhang et al., 2020; Ren et al., 2021), which are not well constrained by ambient atmospheric observations. And compared to studies focusing on individual pollution episodes or short-term case analyses, a long-term statistical perspective enables the identification of systematic and persistent precursor–$PM_{2.5}$ relationships under real atmospheric conditions.

In studies of $PM_{2.5}$ pollution formation, concentrations are jointly shaped by local accumulation processes and regional transport governed by atmospheric circulation patterns (Cheng et al., 2015). The relative contributions of these two factors vary substantially across space and time (Zhang et al., 2014; Ma et al., 2017), such that long-term observational datasets aggregate periods governed by distinct physical and chemical regimes. To address the challenge of isolating precursor-specific $PM_{2.5}$ responses under ambient conditions, we construct an episode-based analysis framework that characterizes local $PM_{2.5}$ accumulation under transport-minimized conditions. This design incorporates the meteorologically informed selection protocol proposed by (Zhu et al., 2021), enabling the isolation of in-situ chemical production processes. Unmeasured variability in primary emissions is further accounted for using carbon monoxide (CO) and coarse particulate matter ($PM_{2.5\text{-}10}$) as emission

https://doi.org/10.5194/egusphere-2026-3211
Preprint. Discussion started: 5 August 2026

proxies. Within this framework, we estimate nonlinear exposure–response functions using shape-constrained additive models (SCAM) and quantify the marginal effects of SO_2 and NO_2 on $PM_{2.5}$ formation across concentration regimes and meteorological conditions.

By providing empirical evidence on regime-dependent precursor sensitivities derived from long-term monitoring data, this study offers a complementary perspective to existing modeling and source apportionment approaches. The results highlight the importance of adaptive and dynamically optimized control strategies, in which precursor mitigation priorities are spatially heterogeneous and continuously adjusted in response to evolving atmospheric conditions.

2 Materials and Methods

2.1 Data and Variables

As part of the broader episode-based experimental design, our analysis focuses on the heating season (November 15 to March 15) from 2016 to 2023 in Beijing. By confining the analysis to this period rather than a full annual cycle, we reduce meteorological confounding and more rigorously satisfy the distributional homogeneity assumptions underlying the statistical models employed. In addition, the heating season is characterized by elevated emissions, which improves the identifiability of source-receptor relationships-a key requirement for the proximal causal inference framework adopted here.

The causal analysis is based on hourly measurements of six conventional air pollutants ($PM_{2.5}$, PM_{10}, SO_2, NO_2, CO and O_3) from 11 monitoring stations operated by the China National Environmental Monitoring Center (CNEMC). $PM_{2.5\text{-}10}$ was obtained as the difference between PM_{10} and $PM_{2.5}$. Meteorological variables, including surface temperature (TEMP), relative humidity (HUMI), wind direction (WD), wind speed (WS), precipitation (RAIN), and atmospheric pressure (PRES), were acquired from the National Meteorological Information Center (http://data.cma.cn/). Hourly boundary layer height (BLH) data were obtained from the ERA5 atmospheric reanalysis of ECMWF and were spatially matched to the nearest monitoring stations.

Following Zhu et al. (2021) and Luo et al. (2022), we applied spatial and temporal processing to the dataset. Stations were grouped into three clusters based on geography and emission characteristics (Fig. 1): a northwestern urban cluster (UrbanNW) with cleaner conditions due to reduced regional transport; a southeastern urban cluster (UrbanSE) comprising more polluted urban sites; and a suburban cluster (Suburban) with lower anthropogenic influence. Temporally, a five-point weighted moving average filter was applied to hourly data to reduce noise, and dust events identified using the algorithm of Tong et al. (2022) were excluded to isolate anthropogenic pollution processes.

2.2 Calm Episode Selection

Following the data segmentation strategy of Zhu et al. (2021) that targets calm intervals after northerly cleansing events, we use a Pollution Dispersion Index (PDI) to rank candidate calm-episode definitions and thereby derive a wind speed threshold tailored to heating-period conditions. The index summarizes local dispersion capacity by combining the ventilation coefficient

https://doi.org/10.5194/egusphere-2026-3211
Preprint. Discussion started: 5 August 2026

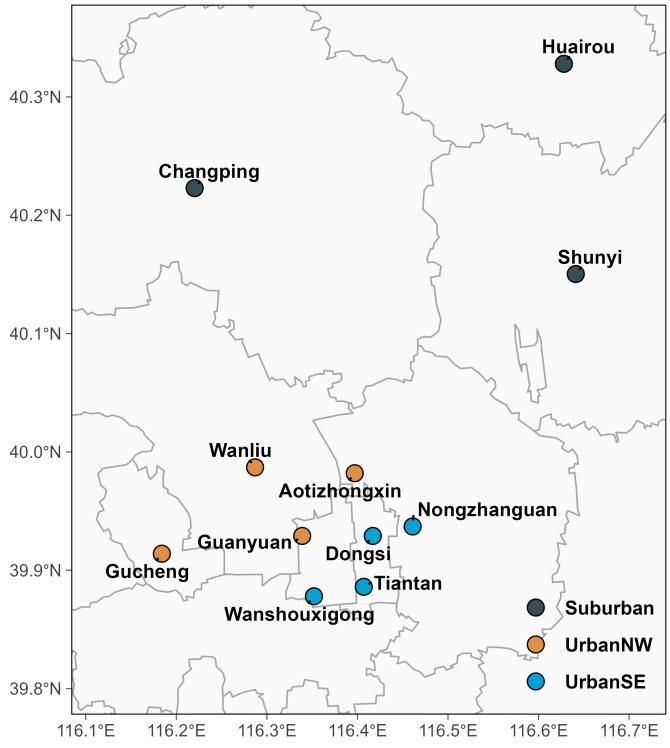

Figure 1. Three site clusters of air quality monitoring stations in Beijing: Suburban (three sites, gray), UrbanNW (four sites, orange), and UrbanSE (four sites, blue).

(VC, defined as the product of wind speed and boundary layer height) with relative humidity (HUMI) to penalize stagnant and humid conditions (Tie et al., 2017; Horton et al., 2012; Yang et al., 2015). The PDI is defined as

$$\mathrm{PDI} = 100 \times \mathbb{E}\left[\mathrm{VC}_{\mathrm{norm}} \times (1 - \mathrm{HUMI}_{\mathrm{norm}})\right], \tag{1}$$

where $\mathrm{VC}_{\mathrm{norm}}$ and $\mathrm{HUMI}_{\mathrm{norm}}$ denote min–max normalized ventilation coefficient and relative humidity, respectively. Lower PDI values indicate episodes with weaker dispersion and are therefore more suitable for isolating local accumulation.

Candidate calm episodes were generated by applying a range of cumulative wind speed thresholds separately to northerly and southerly wind components. The combination giving the lowest mean PDI was selected, corresponding to $\mathrm{CN}_{\mathrm{thres}} = 3.3$ m s^{-1} and $\mathrm{CS}_{\mathrm{thres}} = 13.8$ m s^{-1}. Summary statistics of the selected calm episodes and the full threshold evaluation are provided in the Sect. S1 and Sect. S4, Fig. S6 of the Supplementary Information (SI).

2.3 Causal Inference with Proxy Variables

We develop a proxy-calibrated causal inference framework to quantify exposure–response relationships that summarize how ambient SO_2 and NO_2 levels translate into episode-level $PM_{2.5}$ outcomes under unmeasured emissions and nonlinear atmo-

https://doi.org/10.5194/egusphere-2026-3211
Preprint. Discussion started: 5 August 2026

spheric processes across the three site clusters in Beijing. Within this framework, SO_2 and NO_2 are treated as integrated exposure variables, with estimated effects representing their cumulative influence on $PM_{2.5}$ accumulation over the course of an episode; for NO_2, this includes both its role as a direct precursor and its involvement in atmospheric oxidation processes (Cheng et al., 2016).

Confounding from regional transport and wet deposition is mitigated by restricting the analysis to calm episodes characterized by the absence of persistent directional winds and precipitation. Concurrent measurements of CO and $PM_{2.5\text{-}10}$ are incorporated as proxy tracers for unmeasured local emission, denoted as $\mathbf{W}$, given their limited chemical reactivity over short timescales (Tie et al., 2017) and that combustion and dust emissions are major contributors to primary $PM_{2.5}$ in Beijing (Srivastava et al., 2021; Park et al., 2022). The assumed causal structure is summarized by the directed acyclic graph (DAG) (Pearl, 2013) shown in Fig. 2.

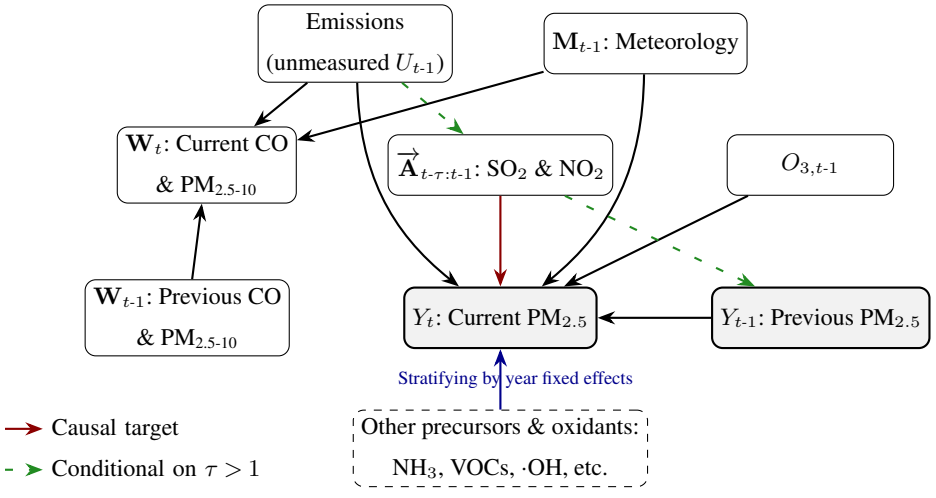

Figure 2. Directed acyclic graph (DAG) summarizing the assumed $PM_{2.5}$ dynamics at time t under calm atmospheric conditions. Solid-frame nodes denote variables explicitly adjusted for in the model, whereas the dashed-frame node denotes unmeasured or slowly varying factors whose long-term influence is partially absorbed by year fixed effects.

We define a generic notation $\vec{V}_{j:t} = (V_j, \ldots, V_t)$ to denote the lagged trajectory of a variable V from time j to t, and introduce a τ-hour lag window to capture the influence of lagged precursor concentrations on $PM_{2.5}$ driven by secondary formation processes. Figure 2 prescribes that under calm conditions, Y_t is influenced by its previous state $Y_{t\text{-}1}$, the lagged precursor trajectory $\vec{\mathbf{A}}_{t-\tau:t\text{-}1}$, local emission intensity $U_{t\text{-}1}$, and meteorological and oxidative conditions $\mathbf{M}_{t\text{-}1}$ and $O_{3,t\text{-}1}$. Here O_3 is treated as a state variable characterizing oxidative conditions.

Given the short duration of typical calm episodes (average 7.6 h, standard deviation 3.2 h), we aggregate the dynamics implied by the DAG to an episode level; the hourly structural equations and the aggregation steps are provided in Sect. S2.1 of the SI. Let i index years (2016—2023) and j index calm episodes within year i. Define the episode-level precursor exposure over a lagged window τ^* that captures the most influential period for secondary $PM_{2.5}$ formation as $\overline{\mathbf{A}}_{ij,\tau^*} = (A_{\mathrm{SO}_2,ij}, A_{\mathrm{NO}_2,ij})^\top$,

https://doi.org/10.5194/egusphere-2026-3211
Preprint. Discussion started: 5 August 2026

the episode-averaged meteorological variables as $\overline{\mathbf{M}}_{ij}$, the episode-averaged ozone concentration as $\overline{O}_{3,ij}$, and the episode duration as L_{ij}. Denote by $Y_{0,ij}$ and Y_{ij} the $PM_{2.5}$ concentrations at episode onset and termination, and by $\mathbf{W}_{0,ij}$, $\mathbf{W}_{ij}$ the corresponding proxy vectors. The episode-level $PM_{2.5}$ outcome and proxy variables are modeled jointly as

$$Y_{ij} = \psi_0 + \boldsymbol{\psi}_A^\top \overline{\mathbf{A}}_{ij,\tau^*} + \boldsymbol{\psi}_M^\top \overline{\mathbf{M}}_{ij} + \psi_Y Y_{0,ij} + \psi_O \overline{O}_{3,ij} + \psi_U \overline{U}_{ij} + \psi_L L_{ij} + \sum_r \psi_r \mathbb{I}(\text{year}_{ij} = r) + \varepsilon_{Y,ij}, \tag{2}$$

$$\mathbf{W}_{ij} = \alpha_0 + \boldsymbol{\alpha}_M^\top \overline{\mathbf{M}}_{ij} + \boldsymbol{\alpha}_W^\top \mathbf{W}_{0,ij} + \alpha_L L_{ij} + \sum_r \alpha_r \mathbb{I}(\text{year}_{ij} = r) + \alpha_U \overline{U}_{ij} + \boldsymbol{\varepsilon}_{W,ij}, \tag{3}$$

where $\overline{U}_{ij}$ represents latent episode-level emission that jointly affects $\mathbf{W}_{ij}$ and Y_{ij}, and $\varepsilon_{Y,ij}$ and $\boldsymbol{\varepsilon}_{W,ij}$ are error terms. The suitable τ^* was determined via a nested model selection procedure based on the Bayesian Information Criterion (BIC). This procedure identified that the cumulative precursor concentrations over the most recent 2–3 hours provided the strongest explanatory power for current $PM_{2.5}$. The selected windows were 2 h for UrbanSE and 3 h for UrbanNW and Suburban as detailed in the SI Sect. S2.4.

An innovation of this work is in extracting emission-related information from the fitted residuals of the proxy Model (3). Let $\widehat{\mathbb{E}}[\cdot]$ denote the fitted regression of Model (3) with the fitted residuals

$$\widetilde{\mathbf{W}}_{ij} = \mathbf{W}_{ij} - \widehat{\mathbb{E}}\left[\mathbf{W}_{ij} \mid \overline{\mathbf{M}}_{ij}, \mathbf{W}_{0,ij}, L_{ij}, \text{year}_{ij}\right], \tag{4}$$

which contains information of the underlying emission $\overline{U}_{ij}$. To reduce potential collinearity, we apply an orthogonal linear transformation to $\widetilde{\mathbf{W}}_{ij}$ to obtain

$$\mathbf{e}_{ij} = \mathbf{P}^\top \widetilde{\mathbf{W}}_{ij}, \tag{5}$$

where $\mathbf{P}$ is a 2×2 orthonormal matrix whose columns consist of the eigenvectors of the sample covariance matrix of the proxy variables $\widetilde{\mathbf{W}}_{ij}$, computed across all episodes. The resulting $\mathbf{e}_{ij}$ are used to substitute the unobservable $\overline{U}_{ij}$ in Model (2), leading to the estimable model for the terminal episode $PM_{2.5}$ outcome

$$Y_{ij} = \psi_0^* + \boldsymbol{\psi}_A^{*\top} \overline{\mathbf{A}}_{ij,\tau^*} + \boldsymbol{\psi}_M^{*\top} \overline{\mathbf{M}}_{ij} + \psi_Y^* Y_{0,ij} + \psi_O^* \overline{O}_{3,ij} + \boldsymbol{\psi}_e^{*\top} \mathbf{e}_{ij} + \psi_L^* L_{ij} + \sum_r \psi_r^* \mathbb{I}(\text{year}_{ij} = r) + \nu_{ij}, \tag{6}$$

where $\boldsymbol{\psi}_A^*$ is the effect of the aggregated precursor exposure over the effective window τ^*, $\boldsymbol{\psi}_M^*$, ψ_Y^*, ψ_O^*, $\boldsymbol{\psi}_e^*$, ψ_L^*, and ψ_r^* are respective coefficients, ψ_0^* denotes the intercept, and ν_{ij} is an error term. Under the standard proxy-variable identification assumptions, the ordinary least squares estimator $\widehat{\boldsymbol{\psi}}_A^*$ provides a consistent estimate of this causal effect; see Sect. S2.2 of the SI for details.

Given the possibly nonlinear evolution of pollutants and the modulation of precursor oxidation by environmental conditions, we extend the linear outcome Model (6) to a generalized additive model (GAM) (Wood, 2017) that accommodates nonlinearity and effect modification (Rothman et al., 2008). To adjust for emission-related confounding, we retain the same proxy-calibration strategy as in (4) and (5), but fit the auxiliary Model (3) via the GAM too. Specifically, for $k = 1, 2$, let $W_{ij}^{(k)}$ denote the episode-ending concentration of proxy k, with $W_{ij}^{(1)} = \text{CO}_{ij}$ and $W_{ij}^{(2)} = \text{PM}_{2.5\text{-}10,ij}$. We fit

$$\mathbb{E}\left[W_{ij}^{(k)} \mid W_{0,ij}^{(k)}, \overline{\mathbf{M}}_{ij}, L_{ij}, \text{year}_{ij}\right] = \alpha_{\text{year}_{ij}}^{(k)} + s_0^{(k)}\left(W_{0,ij}^{(k)}\right) + \sum_{M \in \overline{\mathbf{M}}} s_M^{(k)}(M_{ij}) + s_L^{(k)}(L_{ij}) \tag{7}$$

https://doi.org/10.5194/egusphere-2026-3211
Preprint. Discussion started: 5 August 2026

and then orthogonalize their residuals to obtain the proxy indices $\mathbf{e}_{ij} = (e_{1,ij}, e_{2,ij})^\top$, which are used as emission-related variables in the nonlinear $PM_{2.5}$ outcome model.

Let $\mathbf{Z}_{ij} = (Y_{0,ij}, \overline{\mathbf{M}}_{ij}, \overline{O}_{3,ij}, L_{ij})$ denote the covariates used to adjust for the initial pollution state, meteorological and oxidative conditions, and episode duration. To allow precursor effects to vary across atmospheric regimes, let $\mathbf{E}^*_{ij} = \{E^*_{SO_2,ij}, E^*_{NO_2,ij}\}$ denote the effect modifiers (VanderWeele, 2009) for SO_2 and NO_2. Candidate modifiers are drawn from $\{\overline{TEMP}, \overline{HUMI}, \overline{O}_3, Y_0\}$, motivated by their well-established roles in secondary inorganic aerosol formation (Brown and Stutz, 2012; Wang et al., 2016; Yang et al., 2020; Ma et al., 2023). We evaluate alternative single-modifier specifications and identify the dominant modifier for each precursor using a bootstrap-based Akaike Information Criterion (AIC) ranking procedure, as detailed in Sect. S3.1 of the SI.

We then model the terminal $PM_{2.5}$ concentration Y_{ij} as an additive function:

$$\begin{aligned}\mathbb{E}[Y_{ij} \mid \overline{\mathbf{A}}_{ij,\tau^*}, \mathbf{Z}_{ij}, \mathbf{e}_{ij}, \mathrm{year}_{ij}] = \beta_{\mathrm{year}_{ij}} + \phi_{SO_2}(A_{SO_2,ij}, E^*_{SO_2,ij}) + \phi_{NO_2}(A_{NO_2,ij}, E^*_{NO_2,ij}) \\ + s_{e_1}(e_{1,ij}) + s_{e_2}(e_{2,ij}) + \sum_{V \in \mathbf{Z} \setminus \mathbf{E}^*} s_V(V_{ij}),\end{aligned} \tag{8}$$

where ϕ_{SO_2} and ϕ_{NO_2} are tensor-product spline smooths (Pya and Wood, 2015) constrained to be non-decreasing with respect to the corresponding precursor, A_{SO_2} or A_{NO_2}. The year-specific intercepts $\beta_{\mathrm{year}_{ij}}$ absorb unobserved interannual heterogeneity, s_{e_1} and s_{e_2} adjust for emission-related variation captured by the orthogonalized proxy indices, and the remaining covariates which are not selected as effect modifiers, denoted as $\mathbf{Z} \setminus \mathbf{E}^*$, enter additively through univariate smooth terms s_V.

Estimation of Models (7) and (8) is performed using the penalized spline smoothing (Marx and Eilers, 1998) as implemented in the `scam` and `mgcv` packages in `R`. Smoothing parameters are selected via the generalized cross-validation (Gu and Wahba, 1991), balancing model goodness-of-fit against complexity through a quadratic roughness penalty. The fitted functions $\widehat{\phi}_{SO_2}$ and $\widehat{\phi}_{NO_2}$ in Model (8) offers $PM_{2.5}$ response surfaces of the two precursors with their respective effect modifiers, while $\hat{s}_{e_1}$ and $\hat{s}_{e_2}$ provide the proxy emission effect, and the remaining $\hat{s}_V$ offer those for the other covariate effects.

To gain insight on how precursor sensitivity varies with the modifier distribution, we consider the marginal effect of a precursor evaluated at the q-th quantiles of its modifier. For SO_2, the sensitivity measure is

$$\theta_{SO_2}(a, q) = \frac{\partial}{\partial a} \widehat{\phi}_{SO_2}\big(a, E^{*(q)}_{SO_2}\big), \tag{9}$$

where $E^{*(q)}_{SO_2}$ is the q-th sample quantile of $E^*_{SO_2,ij}$ for a $q \in (0,1)$. The sensitivity measure can be estimated by the differencing method:

$$\widehat{\theta}_{SO_2}(a, q) = \frac{\widehat{\phi}_{SO_2}\big(a+\delta, E^{*(q)}_{SO_2}\big) - \widehat{\phi}_{SO_2}\big(a-\delta, E^{*(q)}_{SO_2}\big)}{2\delta}, \tag{10}$$

where δ is set as a fraction of the interquartile range of the SO_2 distribution to balance numerical stability and local approximation. That for NO_2 can be obtained similarly.

The marginal effect of a precursor, say SO_2, is obtained by averaging the predicted $PM_{2.5}$ response over all episodes while fixing SO_2 at a given level a. Under the sum-to-zero identifiability constraints of the GAM (Wood, 2017), the contributions

https://doi.org/10.5194/egusphere-2026-3211
Preprint. Discussion started: 5 August 2026

from other additive terms than SO_2 (i.e., those containing $A_{NO_2,ij}$, $\mathbf{Z}_{ij}$, and $\mathbf{e}_{ij}$) average to zero across episodes. Consequently, the estimate is given by

$$\widehat{Y}_{SO_2}(a) = \frac{1}{n}\sum_i \sum_{j=1}^{n_i} \hat{\beta}_{\text{year}_{ij}} + \frac{1}{n}\sum_i \sum_{j=1}^{n_i} \widehat{\phi}_{SO_2}(a, E^*_{SO_2,ij}), \tag{11}$$

where $n = \sum_i n_i$ and n_i is the number of episodes in year i. The marginal effect function $\widehat{Y}_{NO_2}(a)$ for NO_2 can be defined similarly, and the joint response when fixing SO_2 at a and NO_2 at b can be estimated as

$$\widehat{Y}(a,b) = \frac{1}{n}\sum_i \sum_{j=1}^{n_i} \hat{\beta}_{\text{year}_{ij}} + \frac{1}{n}\sum_i \sum_{j=1}^{n_i} \left[\widehat{\phi}_{SO_2}(a, E^*_{SO_2,ij}) + \widehat{\phi}_{NO_2}(b, E^*_{NO_2,ij})\right]. \tag{12}$$

3 Results and Discussion

We report major findings on the emission proxies, the effect modifiers governing SO_2 and NO_2 responses, and the resulting nonlinear, regime-dependent precursor–$PM_{2.5}$ relationships. We also present empirical support to the model specification of Model (8) by showing how the proxy-based emission adjustment, nonlinear specification, and effect-modification structure improve the modeling of terminal episode $PM_{2.5}$.

3.1 Proxy indices capture emission-related variation in $PM_{2.5}$

By regressing CO and $PM_{2.5\text{-}10}$ ($\mathbf{W}$) on the meteorological and other covariates as prescribed in (4), we obtained the fitted residual $\widetilde{W}_{ij}$ and then orthogonalized them to separate the residual proxy variation into a shared component e_1 and a contrast e_2.

Figure 3 displays the terminal $PM_{2.5}$ versus the constructed proxy indices e_1 and e_2, together with the fitted component functions $\hat{s}_{e_1}$ and $\hat{s}_{e_2}$, which characterize the partial effects of the emission proxies on $PM_{2.5}$. Both e_1 and e_2 were positively associated with $PM_{2.5}$, as shown in Fig. 3a, indicating that the residual proxy variation contained $PM_{2.5}$-relevant information after reducing confounding by meteorology and initial pollution levels. The Pearson correlation coefficients were 0.41–0.51 for e_1 and 0.41–0.50 for e_2 across the three site clusters, with all of them statistically significant at the 0.001 level.

The first proxy index, e_1, represents the shared residual variability of CO and $PM_{2.5\text{-}10}$ after removing the influences of meteorology, initial conditions, episode duration, and year effects. This interpretation is supported by its positive correlations with both residualized CO and residualized $PM_{2.5\text{-}10}$ across clusters, with Pearson correlation coefficients being 0.77–0.79 and 0.73–0.77, respectively. The second proxy index, e_2, represents a contrast between combustion-related signals and coarse-particle-related emissions, as it was positively correlated with residualized CO (0.64–0.69) and negatively correlated with residualized $PM_{2.5\text{-}10}$ (-0.64 to -0.61). Additional correlation statistics among the proxy indices, residualized proxy variables, and observed pollutant concentrations are given in Sect. S4, Table S1 of the SI.

The estimated partial effects $\hat{s}_{e_1}$ and $\hat{s}_{e_2}$ were nearly linear and positive, with some curvature for $\hat{s}_{e_2}$ in the urban clusters. Over the central 95% of the empirical distribution of e_1, the fitted contribution to terminal $PM_{2.5}$ increased by 43.4, 36.5, and 33.0 $\mu g\,m^{-3}$ in the Suburban, UrbanNW, and UrbanSE clusters, respectively; the corresponding increases for e_2 were 33.2,

https://doi.org/10.5194/egusphere-2026-3211
Preprint. Discussion started: 5 August 2026

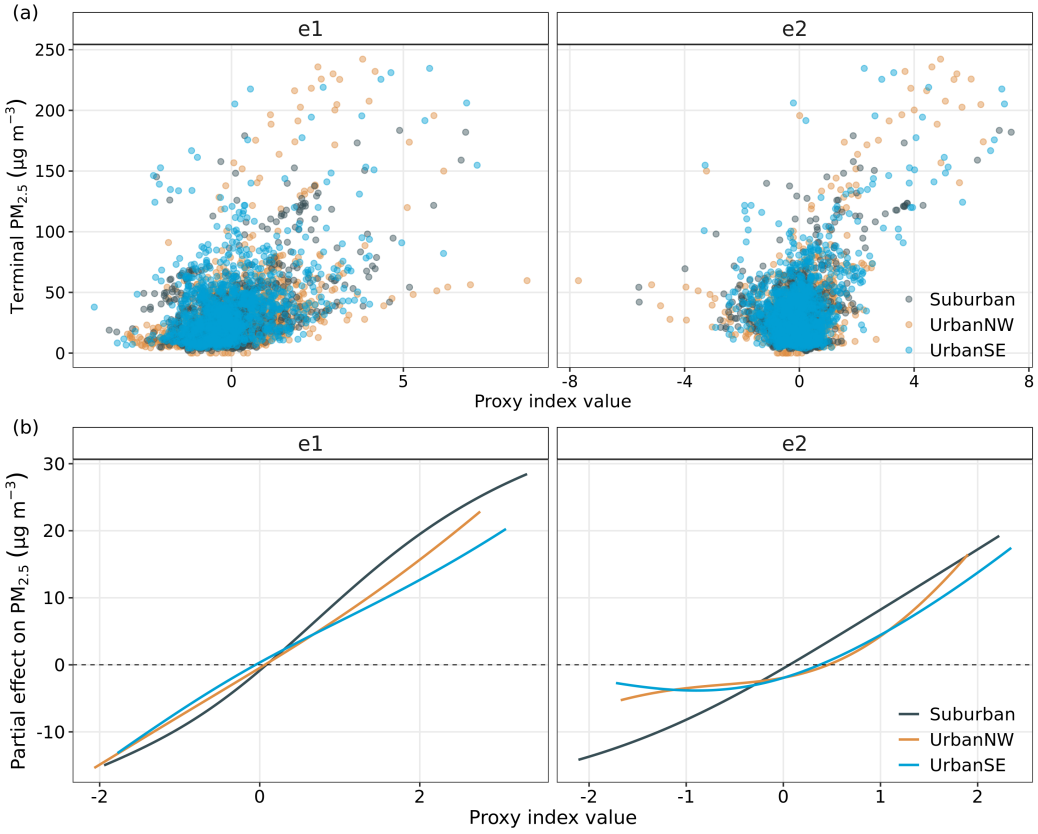

Figure 3. Scatter plots of terminal episode $PM_{2.5}$ concentration versus the two emission proxy indices e_1 and e_2 (a) and the fitted partial effects s_{e_i} in Model (8) (b) for the three site clusters.

23.2, and 22.1 $\mu g\,m^{-3}$. These results indicate that, after adjustment for meteorological and oxidative conditions, emission-related variability exhibited an approximately linear association with $PM_{2.5}$ and that emission sensitivity was the strongest in the suburban area. The positive fitted effect of e_2 further indicates that, after separating the shared emission captured by e_1, the $PM_{2.5}$ was more strongly associated with the residual variability aligned with CO than with that of $PM_{2.5\text{-}10}$.

We assess the role of proxy adjustment by comparing Model (8) with a reduced version that excluded e_1 and e_2. It is shown that incorporating the proxy indices substantially improved model performance across all site clusters. In the Suburban cluster, the inclusion of the proxy terms increased R^2 from 0.742 to 0.902 and reduced the RMSE by approximately 6 $\mu g\,m^{-3}$ (39.1%). For the UrbanNW site cluster, R^2 increased from 0.719 to 0.880 and the RMSE decreased by 5.6 $\mu g\,m^{-3}$ (35.2%). The improvement was more moderate in UrbanSE where R^2 increased from 0.727 to 0.845 and RMSE decreasing by 4.0 $\mu g\,m^{-3}$ (25.0%). These consistent improvements support the effectiveness of the proxy adjustment strategy in capturing emission-related residual variability that are not explained by meteorological and oxidative conditions.

https://doi.org/10.5194/egusphere-2026-3211
Preprint. Discussion started: 5 August 2026

3.2 Oxidative and thermodynamic regimes regulate precursor effectiveness

The conversion of SO_2 and NO_2 to the fine particulate matter is modulated by meteorological and oxidative conditions through multiple chemical processes. We model these processes via the effect modifiers as in Model (8). Candidate modifiers included TEMP, HUMI, O_3, and initial $PM_{2.5}$ concentration (Y_0), which are known for their roles in the secondary aerosol formation. This led to a total of 16 candidate modifier pairs (E_{SO_2}, E_{NO_2}) and 16 bivariate additive components $\phi_{SO_2}(A_{SO_2}, E_{SO_2})$ and $\phi_{NO_2}(A_{NO_2}, E_{NO_2})$ in Model (8). To find the best effect modifier pair, we computed the AIC model selection criterion that balanced the model goodness-of-fit and the number of smoothing spline terms used.

Figure 4 reports the relative AIC improvement scores for all 16 candidate pairs against the no-modifier version of Model (8). To make the selected effect modifiers reflect dominant chemical drivers rather than accidental features of the observed episode sample, we conducted 500 bootstrap random re-generation of the original episodes for each site cluster. The AIC improvement score was defined as the average of the AIC improvement scores across the bootstrap resampled episodes and the three site clusters for each modifier pair. It shows that across all candidate pairs, models with bivariate precursor–modifier consistently outperformed the no-modifier version with reduced average AIC scores. Among the 16 modifier pairs, the SO_2–TEMP and NO_2–O_3 alliance yielded the lowest average AIC score, leading to their selection as the chosen effect-modification structure. These two quite stable effect modifiers reveal that oxidative capacity and thermodynamics are the key drivers of wintertime secondary $PM_{2.5}$ formation.

Temperature was selected as the modifier for SO_2 (Fig. 4b) and the second-ranked modifier for NO_2 after O_3 (Fig. 4c). These indicate the thermodynamic sensitivity of the dominant chemical pathways for the conversion of these two precursors. For SO_2, low temperature favors aqueous and interfacial oxidation pathways (Cheng et al., 2016; Liu et al., 2020), including manganese-catalysed SO_2 oxidation on aerosol surfaces (Wang et al., 2021), whereas warmer conditions generally favors gas-phase oxidation through faster OH-related reaction kinetics and enhanced photochemical radical production (Seinfeld and Pandis, 2016). The temperature modification of SO_2 therefore reflected the importance of multiphase versus gas-phase pathways in sulfate formation.

The temperature modification for NO_2 also reflected the diurnal shift in oxidative pathways. In our data, temperature correlated strongly negatively with the night-time fraction ($\rho = -0.514$, $p < 0.001$). The production and loss of NO_2 were closely tied to photochemistry, with a shift from daytime OH-driven nitrate formation (Chen et al., 2020) to nocturnal NO_3/N_2O_5 chemistry (Brown and Stutz, 2012). This diurnal shift implies that the temperature modification of NO_2 can not be attributed to the thermal sensitivity of a single dominant reaction.

The selection of O_3 as the stable modifier (Fig. 4c) indicates that NO_2 conversion was primarily regulated by oxidative capacity, consistent with the tight chemical coupling between NO_2 and the O_3-NO_x system. NO_2 photolysis is a primary daytime source of ozone, while at night, reactions between NO_2 and O_3 control the formation of NO_3 radicals and N_2O_5 (Brown and Stutz, 2012), which are key intermediates in heterogeneous nitrate production. The calm episodes selected in this study were predominantly within the oxidant-deficient regime defined by Feng et al. (2021), where nitrate formation was sensitive to variations in O_3 levels. Under higher O_3 conditions, enhanced NO_3/N_2O_5 chemistry promotes efficient nocturnal nitrate formation,

https://doi.org/10.5194/egusphere-2026-3211
Preprint. Discussion started: 5 August 2026

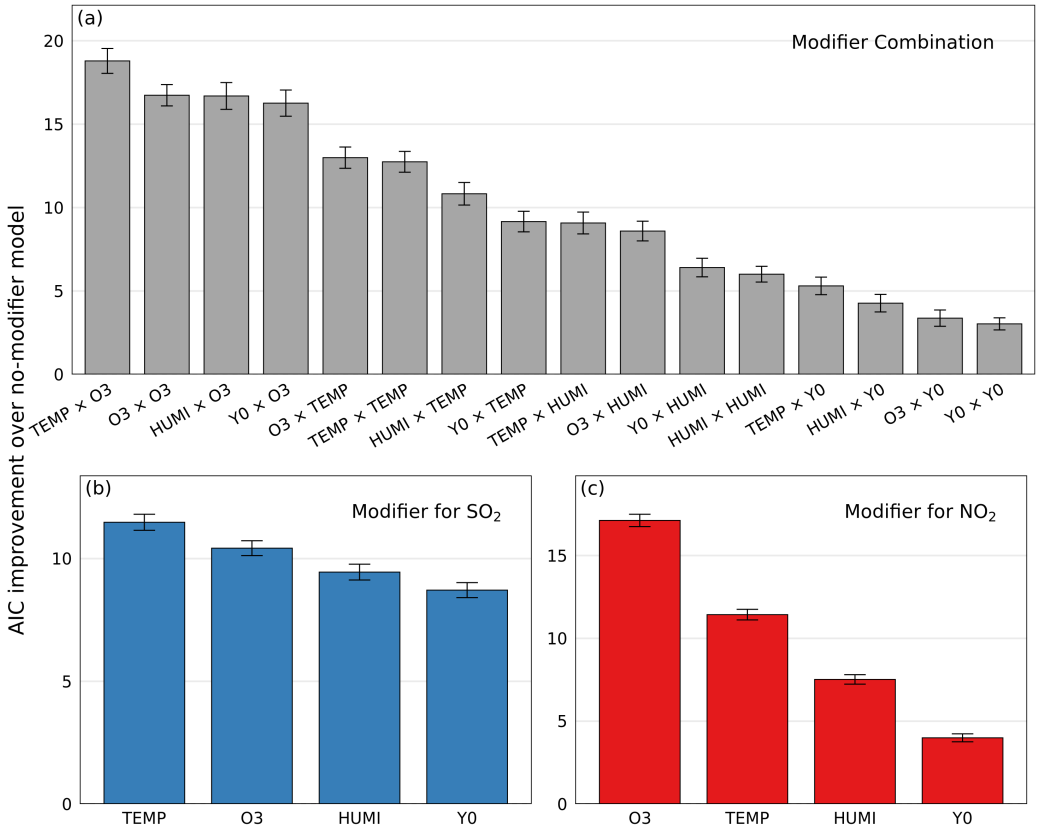

Figure 4. AIC improvement scores for all 16 candidate effect-modification pairs relative to models without effect-modifiers within Model (8) (a) and those for the SO_2 modifiers (b) and the NO_2 modifiers (c), with the error bars indicating ± 1 standard error, obtained from 500 bootstrap episode replications and the three site clusters.

whereas under O_3-limited conditions, NO_2 may even exhibit neutral or negative associations with nocturnal nitrate formation (Ma et al., 2023), a behavior that departs from the non-decreasing shape constraint imposed on the precursor–response function. Ozone also emerged as an effective modifier of SO_2 effects , even though laboratory evidence did not support a direct role of ozone in enhancing SO_2 oxidation efficiency (Jiang, 2010; Sun et al., 2014). This inconsistency suggests that O_3 more plausibly functions as a regime-level indicator of prevailing oxidative conditions that modulate precursor effectiveness (Feng et al., 2021; Liu et al., 2021b).

In contrast, humidity and Y_0 showed less stable modification. Humidity during most calm episodes remained below the 60% phase-transition threshold (Tie et al., 2017; Song et al., 2019). The less stable modifying effect implies that, in this semisolid particle state, the effect of humidity on precursor conversion may be weak or highly nonlinear, making it difficult to capture consistently with the chosen smooth terms. For the pre-existing particle surface area Y_0, the attenuated stability may arise

https://doi.org/10.5194/egusphere-2026-3211
Preprint. Discussion started: 5 August 2026

because its modifying role is confounded with other co-varying factors such as oxidant availability and particle acidity (Cheng et al., 2016; Liu et al., 2021a). As a single scalar, Y_0 does not fully represent the chemical state of the aerosol.

3.3 NO_2-dominant $PM_{2.5}$ response and regime-dependent SO_2 effects under winter calm conditions

We estimated the marginal effects of SO_2 and NO_2 on terminal $PM_{2.5}$ and examined their spatial heterogeneity and temporal trends. The response curves were computed using the estimates given in Eq. (11) for SO_2 and similarly for NO_2. To avoid model extrapolation, we restricted predictions to exposure levels that actually occurred across all episode duration strata ($L = 4$–16 hours). This overlap restriction gave admissible ranges of 2–8 μg m^{-3} for SO_2 and 18–58 μg m^{-3} for NO_2.

3.3.1 Spatial heterogeneity in the effects of sulfate and nitrate precursors on $PM_{2.5}$ accumulation

Figure 5 shows the estimated terminal $PM_{2.5}$ responses as functions of precursor concentrations. The marginal effects for SO_2 and NO_2 (denoted $\widehat{Y}_{\mathrm{SO_2}}(a)$ and $\widehat{Y}_{\mathrm{NO_2}}(a)$) and their joint response surface $\widehat{Y}(a,b)$ were obtained by fixing the respective precursor levels while averaging over the other covariates according to Eqs. (11) and (12).

Within the current concentration regime, NO_2 reductions dominated the expected $PM_{2.5}$ benefit in Suburban and UrbanNW, whereas SO_2 and NO_2 reductions yielded comparable benefits in UrbanSE. Reducing NO_2 from 58 to 18 μg m^{-3} lowered the estimated terminal $PM_{2.5}$ by 11.0, 20.3, and 5.1 μg m^{-3} in Suburban, UrbanNW, and UrbanSE, respectively, whereas reducing SO_2 from 8 to 2 μg m^{-3} lowered $PM_{2.5}$ by 4.3, 3.0, and 5.2 μg m^{-3}, respectively.

The SO_2 response exhibited a mildly increasing slope over its empirical range, meaning that $PM_{2.5}$ sensitivity to SO_2 was higher when SO_2 concentrations were elevated. The weaker slope at low SO_2 levels was consistent with Beijing's air-quality trajectory: rapid $PM_{2.5}$ improvement during the early SO_2 decline was followed by slower gains after SO_2 reached a low baseline. Mechanistically, the attenuated response at low SO_2 may reflect a combination of enhanced oxidant-driven conversion that partly offsets reduced precursor supply (Zhao et al., 2025), reduced new particle formation (Kulmala et al., 2014; Chu et al., 2019), and shifts in sulfur gas–particle partitioning (Lan et al., 2024).

The relative magnitudes of the two precursors' effects differed across the site clusters. UrbanNW showed the largest NO_2 response and the weakest SO_2 response, indicating that $PM_{2.5}$ accumulation there was primarily governed by reactive nitrogen chemistry. UrbanSE, in contrast, exhibited the weakest NO_2 response, consistent with its central urban location where high NO_x emissions and strong O_3 titration suppress nitrate formation pathways. The high NO_2/O_3 ratio at UrbanSE (mean 2.1, SD 3.7) fell within the O_3-limited regime proposed by Ma et al. (2023), where N_2O_5 hydrolysis was suppressed. Nevertheless, the preserved SO_2 responsiveness indicated that sulfur oxidation pathways remained active, as sulfate formation is less directly constrained by O_3 availability.

In Suburban, the fitted responses indicated relatively stronger local sensitivity to SO_2 than to NO_2, especially at higher concentrations. The bivariate density estimates showed that high SO_2 and high NO_2 episodes tended to co-occur in this cluster (SI Sect. S4, Fig. S9a). Under such conditions, competition for neutralizing ammonium may influence the relative formation efficiencies of sulfate and nitrate, because sulfate is preferentially neutralized over nitrate when available NH_4^+ is constrained (Chen et al., 2021). Although regional NH_3 levels in the North China Plain are generally sufficient to sustain secondary

https://doi.org/10.5194/egusphere-2026-3211
Preprint. Discussion started: 5 August 2026

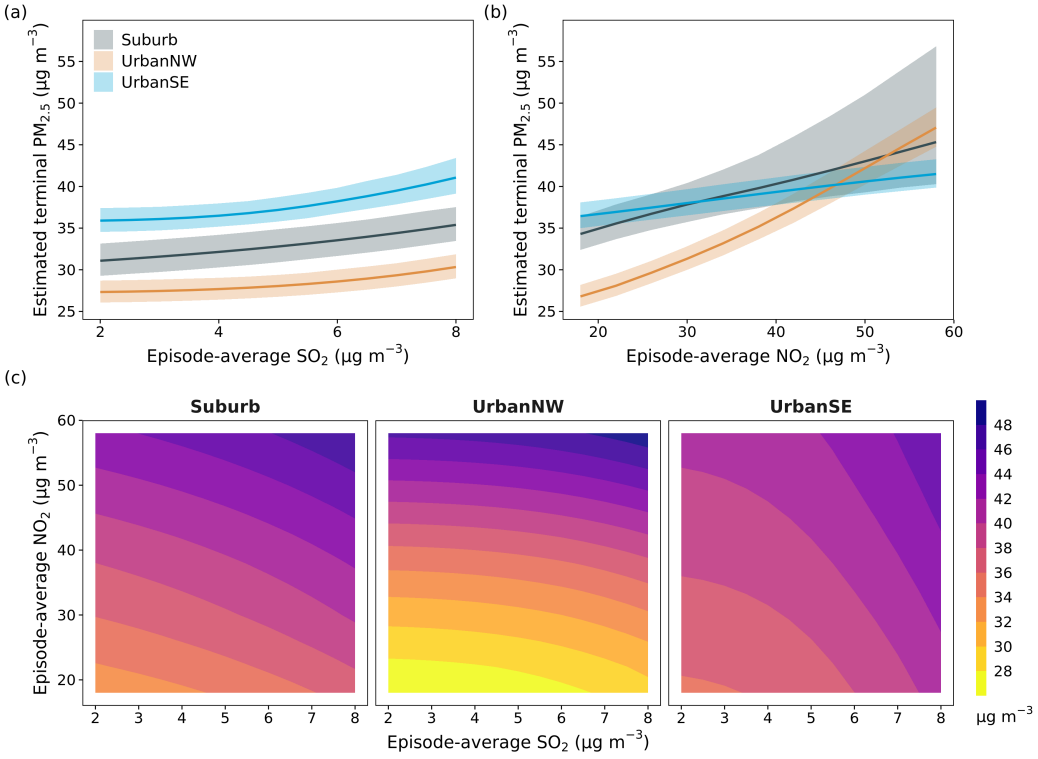

Figure 5. Estimated responses of terminal $PM_{2.5}$ to SO_2 (a) and NO_2 (b) during winter calm episodes, with shaded ribbons indicating 95% bootstrap confidence intervals, and the joint response surface under simultaneous fixation of SO_2 and NO_2 (c), with filled contours representing the estimated terminal $PM_{2.5}$.

inorganic aerosol formation at the system scale (Xing et al., 2018; Lim et al., 2020), the relatively short episode durations in our analysis (mostly ≤ 9 h) implied that the estimated exposure–response relationships primarily reflected near-term responses where local ammonium depletion may preferentially attenuate nitrate formation.

The joint response surfaces in Fig. 5c further illustrate the SO_2 and NO_2 trade-off in $PM_{2.5}$ formation. In UrbanSE, the broad, curved contours indicated weak overall precursor sensitivity but a concentration-dependent trade-off: the relative cost-effectiveness of controlling each precursor varied with their ambient concentration levels. In Suburban, the contours were more densely spaced and closer to straight diagonal lines, suggesting an approximately proportional trade-off. A support-wide average slope indicated that a 1 μg m^{-3} reduction in SO_2 yielded roughly the same $PM_{2.5}$ benefit as a 2.58 ± 0.67 μg m^{-3} reduction in NO_2. UrbanNW showed a contrasting pattern. The contours varied mainly along the NO_2 dimension, reinforcing the single-precursor result that $PM_{2.5}$ responses were dominated by NO_2 variability. In per-unit terms, however, the two precursors had comparable marginal effects: a 1 μg m^{-3} reduction in SO_2 gave roughly the same benefit as a 1.06 ± 0.74 μg m^{-3} reduction in NO_2.

https://doi.org/10.5194/egusphere-2026-3211
Preprint. Discussion started: 5 August 2026

3.3.2 Regime-dependent modification of precursor sensitivity

We further examined how temperature and O_3 levels modify the SO_2 and NO_2 responses. Following Eq. (10), the marginal effect curves were evaluated at selected percentiles $q \in \{10\%, 25\%, 50\%, 75\%, 90\%\}$ of TEMP (for SO_2) and O_3 (for NO_2). Figure 6 shows how precursor sensitivity changes with precursor concentration and modifier level across site clusters.

The modifying role of O_3 on NO_2 was consistent across clusters: NO_2 sensitivity increased with O_3 levels, reflecting that the per-unit increase in NO_2 had a stronger effect on $PM_{2.5}$ formation under enhanced oxidative capacity. In UrbanNW, the effect modification by O_3 was most pronounced.

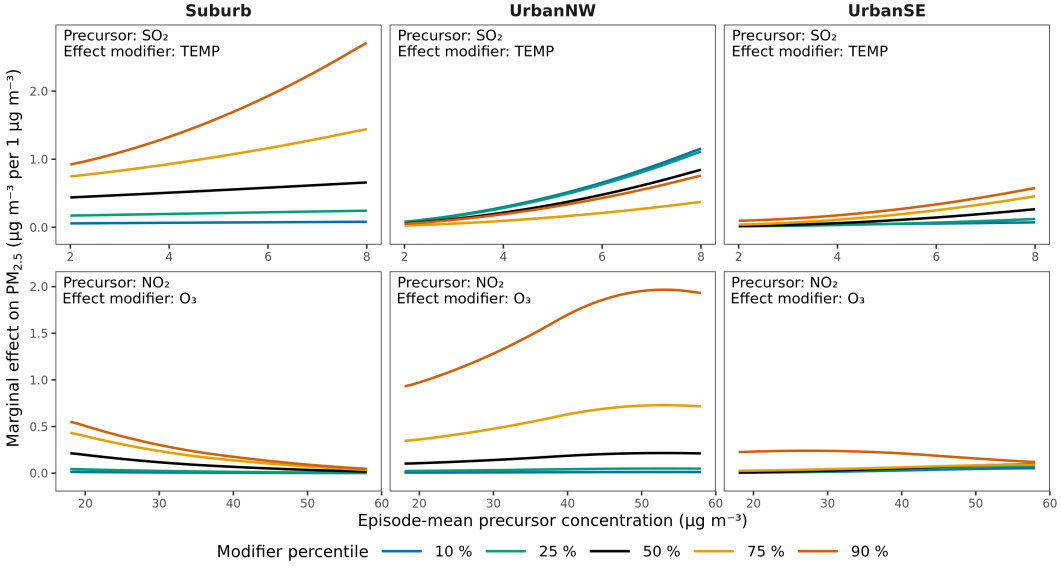

Figure 6. Marginal effects of SO_2 and NO_2 on $PM_{2.5}$ evaluated at selected percentiles of the corresponding effect modifier (indicated by color).

Temperature modified SO_2 effects in a regime-dependent manner. In Suburban and UrbanSE, where SO_2 sensitivity was comparable to or greater than that of NO_2, the SO_2 effect increased with temperature. This positive modification was strongest in Suburban, likely reflecting its higher O_3 levels and more photochemically active conditions. Under such conditions, warmer temperatures may enhance SO_2 oxidation through faster reaction kinetics and greater oxidant availability, including a larger potential contribution from gas-phase OH oxidation.

UrbanNW showed a different pattern. The SO_2 effect increased at higher temperatures but also strengthened during very cold episodes. This non-monotonic modification would not arise from simple covariation, indicating a plausible shift in the dominant chemical regime. UrbanNW showed the strongest marginal effect of NO_2 across Beijing, suggesting that reactive nitrogen chemistry was more likely to interact with sulfur oxidation pathways than in other site clusters. Low temperatures thermodynamically favour the stability of N_2O_5 and the partitioning of NH_3 and HNO_3 into particulate ammonium nitrate

https://doi.org/10.5194/egusphere-2026-3211
Preprint. Discussion started: 5 August 2026

(Behera and Sharma, 2010; Dong et al., 2020; Balamurugan et al., 2022). The resulting increase in aerosol liquid water associated with hygroscopic nitrate salts can enhance multiphase reactivity (Liu et al., 2021a), facilitating heterogeneous uptake and aqueous-phase SO_2 oxidation, including pathways involving NO_2 (Cheng et al., 2016; Wang et al., 2016). The strengthened SO_2 response during the coldest episodes may therefore indicate a greater role of heterogeneous and aqueous-phase sulfur oxidation in UrbanNW.

3.3.3 Early SO_2 gains and increasing NO_2 effects on $PM_{2.5}$ improvement after 2016

To quantify precursor-associated $PM_{2.5}$ changes after 2016, we constructed duration-standardized responses. For each year r, precursor p, and episode duration stratum L, we evaluated the fitted precursor-specific smooth $\widehat{\phi}_p(A_p, E_p^*)$ by pairing the observed A_p values from year r within stratum L with modifier values E_p^* drawn from the pooled 2016—2023 empirical distribution conditional on stratum L. The resulting stratum-specific responses were then averaged using the pooled 2016—2023 duration distribution as reference weights. The precursor-associated $PM_{2.5}$ change for year r was defined as the difference between the resulting standardized response and its 2016 counterpart. Implementation details are provided in the Sect. S3.4 of the SI.

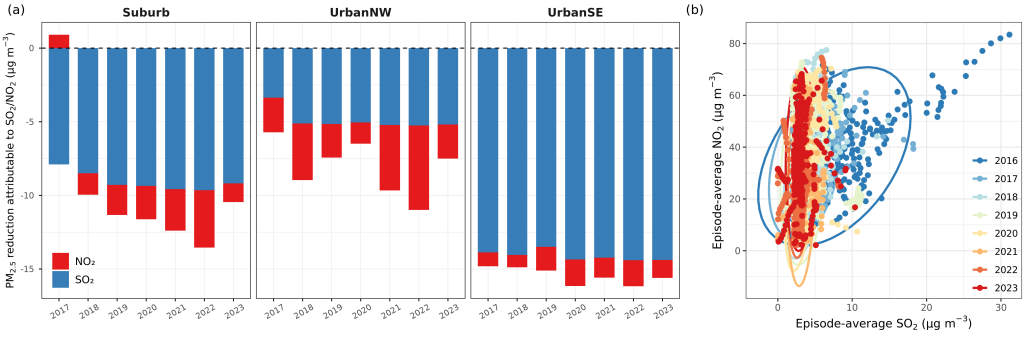

Figure 7. Estimated changes in $PM_{2.5}$ relative to 2016 attributable to SO_2 (blue) and NO_2 (red) reductions (a), and scatter plot of episode-average SO_2 and NO_2 concentrations with year-specific 95% concentration ellipses, 2016–2023 (b).

Figure 7 shows the estimated changes in $PM_{2.5}$ relative to 2016 attributable to precursor reductions, alongside the joint distribution of SO_2 and NO_2 concentrations during calm episodes from 2016 to 2023. Across all clusters, the largest reduction occurred between 2016 and 2017, after which the estimated terminal $PM_{2.5}$ levels of calm episodes remained relatively stable. SO_2 reductions accounted for the larger share of the precursor-associated $PM_{2.5}$ decrease in most clusters and years. This dominance was most pronounced in UrbanSE, where the estimated SO_2-associated reduction reached 13–14 μg m^{-3} relative to 2016 and remained substantially larger than the NO_2 contribution throughout the study period. A similar but weaker pattern appeared in the Suburban cluster, with SO_2-associated contrasts stabilizing at 8–10 μg m^{-3} after 2016. In UrbanNW, the SO_2-associated reduction stayed below about 5 μg m^{-3} over the entire period.

https://doi.org/10.5194/egusphere-2026-3211
Preprint. Discussion started: 5 August 2026

The relative contribution of NO_2 reductions was smaller overall but increased after 2020, especially in UrbanNW. Although SO_2 explained most of the early $PM_{2.5}$ improvement in this cluster, the NO_2-associated reduction grew substantially during 2021–2022 and became comparable to that of SO_2. However, a modest rebound of NO_2 concentrations in 2023 led to corresponding increases in NO_2-attributable $PM_{2.5}$ across all three clusters, with estimated increments of 0.5–3.4 μg m^{-3} relative to 2022.

3.4 Model performance and robustness

To assess whether the resulting model specification provided an adequate representation of $PM_{2.5}$ accumulation during calm episodes, we evaluated the predictive performance of the fitted outcome model and the incremental contribution of the nonlinear and proxy-adjusted specifications.

Table 1 presents the R^2 and RMSE for linear and nonlinear models under different specifications across the three site clusters. The fitted Model (8) yielded adjusted R^2 values of 0.903, 0.880, and 0.845 and RMSE values of 9.3, 10.3, and 12.0 $\mu\mathrm{g\,m^{-3}}$ for Suburban, UrbanNW, and UrbanSE, respectively. Compared to its linear counterpart using the same covariate set and interaction structure, the nonlinear full model increased R^2 by 0.045–0.074 and reduced RMSE by 2.4–3.1 $\mu\mathrm{g\,m^{-3}}$ (19%–23%) across the three clusters. Within the nonlinear framework, adding the proxy indices further increased adjusted R^2 by 0.118–0.161 and reduced RMSE by 4.0–6.0 $\mu\mathrm{g\,m^{-3}}$.

Leave-one-episode-out cross-validation provided an assessment of out-of-sample generalizability. The RMSE differences between the nonlinear full model and the linear full model were +2.18, +0.12, and –0.11 $\mu\mathrm{g\,m^{-3}}$ for Suburban, UrbanNW, and UrbanSE, respectively (positive values indicate higher error for the nonlinear model). These comparable RMSEs indicate that the improved in-sample fit of the nonlinear specification does not come at the cost of substantially reduced predictive generalizability.

Table 1. The adjusted R^2 and the root mean square errors (RMSE) in parentheses for various model structures with respect to proxy-based emission adjustment, effect modification, and nonlinear specification across the three site clusters.

	Linear model		Nonlinear model		
Site cluster	Without proxy	Full model	Without proxy	Without modifier	Full model
Suburban	0.611 (19.3)	0.858 (11.7)	0.742 (15.3)	0.883 (10.2)	0.903 (9.3)
UrbanNW	0.591 (19.5)	0.806 (13.4)	0.719 (15.9)	0.865 (11.0)	0.880 (10.3)
UrbanSE	0.597 (19.8)	0.775 (14.8)	0.727 (16.0)	0.827 (12.7)	0.845 (12.0)

For the linear model, the full model includes the proxy terms and linear precursor–modifier interaction terms. For the nonlinear model, the full specification is given by Model (8). The nonlinear model without modifier includes the same proxy terms but replaces the bivariate precursor–modifier smooths with separate shape-constrained univariate smooth terms for the precursors and univariate smooth terms for the selected modifiers.

https://doi.org/10.5194/egusphere-2026-3211
Preprint. Discussion started: 5 August 2026

Although the linear full specification already achieved reasonable model fit (adjusted R^2 ranging from 0.775 to 0.858), the extension to the nonlinear GAM framework further improved the model goodness-of-fit without appreciably sacrificing predictive generalizability, as evidenced by the consistent cross-validation performance.

We also tested a GAM specification using the same covariates as Model (8) but with univariate smooth functions for all covariates. Incorporating effect modification further enhanced the nonlinear proxy-adjusted models, increasing R^2 by 0.015–0.020 and reducing RMSE by 0.7–0.9 $\mu g\,m^{-3}$ relative to the corresponding non-interaction specifications; see Sect. S3.3 of the SI for explicit formulas of each model specification, and Figs. S7 and S8 in Sect. S4 for the fitted smooth terms of the final outcome model.

4 Conclusions

Using routine monitoring data from Beijing winter heating seasons during 2016–2023, this study develops an episode-based framework to quantify the effects of ambient SO_2 and NO_2 on $PM_{2.5}$ accumulation under dispersion-limited conditions. By restricting the analysis to calm episodes and using CO and $PM_{2.5\text{-}10}$ as proxies for unresolved emissions, the framework reduces the influence of regional transport and primary-emission confounding, allowing precursor sensitivities to be estimated under relatively homogeneous atmospheric conditions.

The analysis identifies a 2–3 h effective exposure window for precursor influence, with a shorter window in the more polluted UrbanSE cluster, suggesting faster apparent secondary processing under pollution-hotspot conditions. Proxy calibration shows that $PM_{2.5}$ variability is mainly associated with combustion-related signals captured by CO, whereas the $PM_{2.5\text{-}10}$-aligned signal is weaker after isolating the shared emission component with CO.

The estimated precursor responses are nonlinear and regime dependent. Ozone is the most stable modifier of NO_2 responses, while temperature is the most stable modifier of SO_2 responses, suggesting that oxidative capacity and thermal conditions are key regulators of precursor effectiveness during winter calm episodes. The magnitude and shape of these responses vary across site clusters. Within the empirically supported concentration range, the SO_2–NO_2 trade-off in $PM_{2.5}$ formation varies spatially, with near-proportional substitution in Suburban, NO_2-dominated responses in UrbanNW, and concentration-dependent marginal substitution in the O_3-limited UrbanSE region.

Annual attribution further shows that SO_2 reductions explain most precursor-associated $PM_{2.5}$ improvements in the early years after 2016, especially in UrbanSE. As ambient SO_2 concentrations decline, the aggregate contribution of further SO_2 reductions weakens, although the per-unit SO_2 response remains comparable to, or locally greater than, that of NO_2. In contrast, the contribution associated with NO_2 reductions increases after 2020 and becomes comparable to SO_2 in UrbanNW during 2021–2022. Together, these patterns suggest a gradual shift toward a more nitrate-sensitive wintertime $PM_{2.5}$ formation regime in Beijing.

Several limitations should be acknowledged. The analysis is restricted to heating-season calm episodes, which generally do not coincide with the most severe pollution accumulation events; thus the extent to which the estimated precursor sensitivities can be generalized to heavily polluted conditions remains uncertain. The inferred chemical interpretation is derived from

https://doi.org/10.5194/egusphere-2026-3211
Preprint. Discussion started: 5 August 2026

long-term observational patterns and should therefore be interpreted as episode-average statistical regularities that incorporate uncertainty, rather than as explicit resolution of a unified chemical pathway operating across individual pollution events.

Overall, the results suggest that future wintertime $PM_{2.5}$ mitigation in Beijing may become increasingly sensitive to NO_x control and oxidative-regime conditions, and that reducing O_3 levels may help weaken the contribution of NO_2 to $PM_{2.5}$ formation. More broadly, the proposed framework demonstrates that routine monitoring data can provide chemically interpretable estimates of regime-dependent precursor sensitivities when transport and emission-related confounding are explicitly addressed.

Code and data availability. The air quality and meteorological data used in this study are available from the China National Environmental Monitoring Center (http://www.cnemc.cn/) and the National Meteorological Information Center (http://data.cma.cn/), respectively. ERA5 boundary layer height data were obtained from the Copernicus Climate Data Store (https://cds.climate.copernicus.eu/). The R code for the SCAM models is available from the corresponding author upon request.

Author contributions. HL and SXC designed the research. HL and XL performed the analyses. HL and SXC wrote the manuscript with input from XL.

Competing interests. The authors declare that they have no conflict of interest.

Acknowledgements. The authors were partially supported by National Natural Science Foundation of China Grants 12292980, 12292983 and 92358303; and Fundamental and Interdisciplinary Disciplines Breakthrough Plan of Ministry of Education of China (No. JYB2025XDXM904).

https://doi.org/10.5194/egusphere-2026-3211
Preprint. Discussion started: 5 August 2026

References

Balamurugan, V., Chen, J., Qu, Z., Bi, X., and Keutsch, F. N.: Secondary $PM_{2.5}$ decreases significantly less than NO_2 emission reductions during COVID lockdown in Germany, Atmospheric chemistry and physics, 22, 7105–7129, https://doi.org/10.5194/acp-22-7105-2022, 2022.

Behera, S. N. and Sharma, M.: Investigating the potential role of ammonia in ion chemistry of fine particulate matter formation for an urban environment, Science of The Total Environment, 408, 3569–3575, https://doi.org/10.1016/j.scitotenv.2010.04.017, 2010.

Brown, S. S. and Stutz, J.: Nighttime radical observations and chemistry, Chemical Society reviews, 41, 6405–6447, https://doi.org/10.1039/C2CS35181A, 2012.

Chen, C., Zhang, H., Yan, W., Wu, N., Zhang, Q., and He, K.: Aerosol water content enhancement leads to changes in the major formation mechanisms of nitrate and secondary organic aerosols in winter over the North China Plain, Environmental Pollution, 287, 117 625, https://doi.org/10.1016/j.envpol.2021.117625, 2021.

Chen, M., Dai, F., Yang, B., and Zhu, S.: Effects of urban green space morphological pattern on variation of $PM_{2.5}$ concentration in the neighborhoods of five Chinese megacities, Building and Environment, 158, 1–15, https://doi.org/10.1016/j.buildenv.2019.04.058, 2019.

Chen, X., Wang, H., Lu, K., Li, C., Zhai, T., Tan, Z., Ma, X., Yang, X., Liu, Y., Chen, S., Dong, H., Li, X., Wu, Z., Hu, M., Zeng, L., and Zhang, Y.: Field Determination of Nitrate Formation Pathway in Winter Beijing, Environmental Science & Technology, 54, 9243–9253, https://doi.org/10.1021/acs.est.0c00972, 2020.

Chen Group: Air Quality Assessment Report for 2013–2024, https://www.songxichen.com/index.php/Research, series report; accessed on 2026-01-03, 2025.

Cheng, N., Li, Y., Zhang, D., Nie, T., Qiu, Q., and Xu, W.: Formation Mechanism of a Serious Pollution Event in January 2013 in Beijing, Environmental Science, 36, 1154–1163, https://doi.org/10.13227/j.hjkx.2015.04.003, 2015.

Cheng, Y., Zheng, G., Wei, C., Mu, Q., Zheng, B., Wang, Z., et al.: Reactive nitrogen chemistry in aerosol water as a source of sulfate during haze events in China, Science Advances, 2, https://doi.org/10.1126/sciadv.1601530, 2016.

Chu, B., Kerminen, V.-M., Bianchi, F., Yan, C., Petäjä, T., and Kulmala, M.: Atmospheric new particle formation in China, Atmospheric Chemistry and Physics, 19, 115–138, https://doi.org/10.5194/acp-19-115-2019, 2019.

Dong, Z., Su, F., Zhang, Z., and Wang, S.: Observation of chemical components of $PM_{2.5}$ and secondary inorganic aerosol formation during haze and sandy haze days in Zhengzhou, China, Journal of Environmental Sciences, 88, 316–325, https://doi.org/10.1016/j.jes.2019.09.016, 2020.

Feng, T., Zhao, S., Bei, N., Liu, S., and Li, G.: Increasing atmospheric oxidizing capacity weakens emission mitigation effort in Beijing during autumn haze events, Chemosphere, 281, 130 855, https://doi.org/10.1016/j.chemosphere.2021.130855, 2021.

Gouveia, N., Kephart, J. L., Dronova, I., McClure, L., Granados, J. T., Betancourt, R. M., et al.: Ambient fine particulate matter in Latin American cities: Levels, population exposure, and associated urban factors, Science of The Total Environment, 772, 145 035, https://doi.org/10.1016/j.scitotenv.2021.145035, 2021.

Gu, C. and Wahba, G.: Minimizing GCV/GML Scores with Multiple Smoothing Parameters via the Newton Method, SIAM Journal on Scientific and Statistical Computing, 12, 383–398, https://doi.org/10.1137/0912021, 1991.

Guo, Z., Shi, L., Chen, S., Jiang, W., Wei, Y., Rui, M., et al.: Sulfur isotopic fractionation and source appointment of $PM_{2.5}$ in Nanjing region around the second session of the Youth Olympic Games, Atmospheric Research, 174-175, 9–17, https://doi.org/10.1016/j.atmosres.2016.01.011, 2016.

https://doi.org/10.5194/egusphere-2026-3211
Preprint. Discussion started: 5 August 2026

Han, C., Xu, R., Ye, T., Xie, Y., Zhao, Y., Liu, H., et al.: Mortality burden due to long-term exposure to ambient $PM_{2.5}$ above the new WHO air quality guideline based on 296 cities in China, Environment International, 166, 107 331, https://doi.org/10.1016/j.envint.2022.107331, 2022.

Horton, D. E., Harshvardhan, and Diffenbaugh, N. S.: Response of air stagnation frequency to anthropogenically enhanced radiative forcing, Environmental research letters, 7, 44 034–9, https://doi.org/10.1088/1748-9326/7/4/044034, 2012.

Jiang, S.: Experimental and Mechanism Study on Multi-pollutants Control by Ozone and Active molecule, Ph.D. thesis, Zhejiang University, 2010.

Kitayama, K., Morino, Y., Yamaji, K., and Chatani, S.: Uncertainties in O_3 concentrations simulated by CMAQ over Japan using four chemical mechanisms, Atmospheric Environment, 198, 448–462, https://doi.org/10.1016/j.atmosenv.2018.11.003, 2019.

Kong, L., Tan, Q., Feng, M., Qu, Y., An, J., Liu, X., et al.: Investigating the characteristics and source analyses of $PM_{2.5}$ seasonal variations in Chengdu, Southwest China, Chemosphere, 243, 125 267, https://doi.org/10.1016/j.chemosphere.2019.125267, 2020.

Kulmala, M., Petäjä, T., Ehn, M., Thornton, J., Sipilä, M., Worsnop, D. R., and Kerminen, V. .: Chemistry of Atmospheric Nucleation: On the Recent Advances on Precursor Characterization and Atmospheric Cluster Composition in Connection with Atmospheric New Particle Formation, Annual Review of Physical Chemistry, 65, 21–37, https://doi.org/10.1146/annurev-physchem-040412-110014, 2014.

Lan, Z., Zhang, X., Lin, W., Xu, X., Ma, Z., Jin, J., Wu, L., and Zhang, Y.: Atmospheric NH_3 in urban Beijing: long-term variations and implications for secondary inorganic aerosol control, Atmospheric chemistry and physics, 24, 9355–9368, https://doi.org/10.5194/acp-24-9355-2024, 2024.

Liang, X., Zou, T., Guo, B., Li, S., Zhang, H., Zhang, S., et al.: Assessing Beijing's $PM_{2.5}$ pollution: severity, weather impact, APEC and winter heating, Proceedings of the Royal Society. A, Mathematical, Physical, and Engineering Sciences, 471, 20150 257, https://doi.org/10.1098/rspa.2015.0257, 2015.

Lim, S., Yang, X., Lee, M., Li, G., Gao, Y., Shang, X., et al.: Fossil-driven secondary inorganic $PM_{2.5}$ enhancement in the North China Plain: Evidence from carbon and nitrogen isotopes, Environmental Pollution, 266, 115 163, https://doi.org/10.1016/j.envpol.2020.115163, 2020.

Liu, P., Ye, C., Xue, C., Zhang, C., Mu, Y., and Sun, X.: Formation mechanisms of atmospheric nitrate and sulfate during the winter haze pollution periods in Beijing: gas-phase, heterogeneous and aqueous-phase chemistry, Atmospheric Chemistry and Physics, 20, 4153–4165, https://doi.org/10.5194/acp-20-4153-2020, 2020.

Liu, Y., Feng, Z., Zheng, F., Bao, X., Liu, P., Ge, Y., et al.: Ammonium nitrate promotes sulfate formation through uptake kinetic regime, Atmospheric Chemistry and Physics, 21, 13 269–13 286, https://doi.org/10.5194/acp-21-13269-2021, 2021a.

Liu, Z., Wang, Y., Hu, B., Lu, K., Tang, G., Ji, D., Yang, X., Gao, W., Xie, Y., Liu, J., Yao, D., Yang, Y., and Zhang, Y.: Elucidating the quantitative characterization of atmospheric oxidation capacity in Beijing, China, The Science of the total environment, 771, 145 306, https://doi.org/10.1016/j.scitotenv.2021.145306, 2021b.

Luecken, D. J., Yarwood, G., and Hutzell, W. T.: Multipollutant modeling of ozone, reactive nitrogen and HAPs across the continental US with CMAQ-CB6, Atmospheric Environment, 201, 62–72, https://doi.org/10.1016/j.atmosenv.2018.11.060, 2019.

Luo, S., Zhu, Y., and Chen, S. X.: Episode based air quality assessment, Atmospheric Environment, 285, 119 242, https://doi.org/10.1016/j.atmosenv.2022.119242, 2022.

Ma, P., Quan, J., Dou, Y., Pan, Y., Liao, Z., Cheng, Z., et al.: Regime-Dependence of Nocturnal Nitrate Formation via N_2O_5 Hydrolysis and Its Implication for Mitigating Nitrate Pollution, Geophysical Research Letters, 50, e2023GL106 183, https://doi.org/10.1029/2023GL106183, 2023.

https://doi.org/10.5194/egusphere-2026-3211
Preprint. Discussion started: 5 August 2026

Ma, Q., Wu, Y., Zhang, D., Wang, X., Xia, Y., Liu, X., et al.: Roles of regional transport and heterogeneous reactions in the $PM_{2.5}$ increase during winter haze episodes in Beijing, The Science of the total environment, 599-600, 246–253, https://doi.org/10.1016/j.scitotenv.2017.04.193, 2017.

Ma, X., Morawska, L., Zou, B., Gao, J., Deng, J., Wang, X., et al.: Towards compliance with the 2021 WHO Air Quality Guidelines: A comparative analysis of $PM_{2.5}$ trends in Australia and China, Environment International, 198, 109 378, https://doi.org/10.1016/j.envint.2025.109378, 2025.

Marx, B. D. and Eilers, P. H.: Direct generalized additive modeling with penalized likelihood, Computational Statistics & Data Analysis, 28, 193–209, https://doi.org/10.1016/S0167-9473(98)00033-4, 1998.

Ouyang, H., Tang, X., Kumar, R., Zhang, R., Brasseur, G., Churchill, B., et al.: Toward Better and Healthier Air Quality: Implementation of WHO 2021 Global Air Quality Guidelines in Asia, Bulletin of the American Meteorological Society, 103, E1696–E1703, https://doi.org/10.1175/BAMS-D-22-0040.1, 2022.

Park, J., Kim, H., Kim, Y., Heo, J., Kim, S.-W., Jeon, K., Yi, S.-M., and Hopke, P. K.: Source apportionment of $PM_{2.5}$ in Seoul, South Korea and Beijing, China using dispersion normalized PMF, Science of The Total Environment, 833, 155 056, https://doi.org/10.1016/j.scitotenv.2022.155056, 2022.

Pearl, J.: Causality: Models, reasoning, and inference, second edition, Cambridge University Press, Cambridge, 2nd edn., ISBN 9780511803161, 2013.

Pya, N. and Wood, S. N.: Shape-constrained additive models, Statistics and Computing, 25, 543–559, https://doi.org/10.1007/s11222-013-9448-7, 2015.

Ren, C., Huang, X., Wang, Z., Sun, P., Chi, X., Ma, Y., et al.: Nonlinear response of nitrate to NOx reduction in China during the COVID-19 pandemic, Atmospheric Environment, 264, 118 715, https://doi.org/10.1016/j.atmosenv.2021.118715, 2021.

Rothman, K. J., Greenland, S., and Lash, T. L.: Modern Epidemiology, Lippincott Williams & Wilkins, Philadelphia, PA, 3rd edn., ISBN 9780781755641, 2008.

Seinfeld, J. H. and Pandis, S. N.: Atmospheric chemistry and physics: from air pollution to climate change, Wiley, Hoboken, New Jersey, 3rd edn., ISBN 9781118947401, 2016.

Song, S., Nenes, A., Gao, M., Zhang, Y., Liu, P., Shao, J., et al.: Thermodynamic Modeling Suggests Declines in Water Uptake and Acidity of Inorganic Aerosols in Beijing Winter Haze Events during 2014/2015–2018/2019, Environmental Science & Technology Letters, 6, 752–760, https://doi.org/10.1021/acs.estlett.9b00621, 2019.

Srivastava, D., Xu, J., Vu, T. V., Liu, D., Li, L., Fu, P., Hou, S., Moreno Palmerola, N., Shi, Z., and Harrison, R. M.: Insight into $PM_{2.5}$ sources by applying positive matrix factorization (PMF) at urban and rural sites of Beijing, Atmospheric Chemistry and Physics, 21, 14 703–14 724, https://doi.org/10.5194/acp-21-14703-2021, 2021.

Sun, C., Zhao, N., Zhuang, Z., Wang, H., Liu, Y., Weng, X., and Wu, Z.: Mechanisms and reaction pathways for simultaneous oxidation of NO_x and SO_2 by ozone determined by in situ IR measurements, Journal of Hazardous Materials, 274, 376–383, https://doi.org/10.1016/j.jhazmat.2014.04.027, 2014.

Sun, Z., Zong, Z., Tian, C., Li, J., Sun, R., Ma, W., et al.: Reapportioning the sources of secondary components of $PM_{2.5}$: A combined application of positive matrix factorization and isotopic evidence, Science of The Total Environment, 764, 142 925, https://doi.org/10.1016/j.scitotenv.2020.142925, 2021.

https://doi.org/10.5194/egusphere-2026-3211
Preprint. Discussion started: 5 August 2026

Tie, X., Huang, R.-J., Cao, J., Zhang, Q., Cheng, Y., Su, H., Chang, D., Pöschl, U., Hoffmann, T., Dusek, U., Li, G., Worsnop, D. R., and O'Dowd, C. D.: Severe Pollution in China Amplified by Atmospheric Moisture, Scientific reports, 7, 15 760–8, https://doi.org/10.1038/s41598-017-15909-1, 2017.

Tong, P., Chen, S., and Tang, C.: Detecting and Evaluating Dust-Events in North China With Ground Air Quality Data, Earth and Space Science, 9, e2021EA001 849, https://doi.org/10.1029/2021EA001849, 2022.

VanderWeele, T. J.: On the Distinction Between Interaction and Effect Modification, Epidemiology, 20, 863–871, https://doi.org/10.1097/EDE.0b013e3181ba333c, 2009.

Wang, G., Zhang, R., Gomez, M. E., Yang, L., Zamora, M. L., Hu, M., et al.: Persistent sulfate formation from London Fog to Chinese haze, Proceedings of the National Academy of Sciences - PNAS, 113, 13 630–13 635, https://doi.org/10.1073/pnas.1616540113, 2016.

Wang, W., Liu, M., Wang, T., Song, Y., Zhou, L., Cao, J., et al.: Sulfate formation is dominated by manganese-catalyzed oxidation of SO_2 on aerosol surfaces during haze events, Nature communications, 12, 1993, https://doi.org/10.1038/s41467-021-22091-6, 2021.

Wood, S. N.: Generalized Additive Models: An Introduction with R, Chapman and Hall/CRC, New York, 2 edn., ISBN 9781315370279, https://doi.org/10.1201/9781315370279, 2017.

World Health Organization: WHO global air quality guidelines: Particulate matter ($PM_{2.5}$ and PM_{10}), ozone, nitrogen dioxide, sulfur dioxide and carbon monoxide, World Health Organization, Geneva, https://www.who.int/publications/i/item/9789240034228, 2021.

Xing, J., Ding, D., Wang, S., Zhao, B., Jang, C., Wu, W., Zhang, F., Zhu, Y., and Hao, J.: Quantification of the enhanced effectiveness of NOx control from simultaneous reductions of VOC and NH3 for reducing air pollution in the Beijing–Tianjin–Hebei region, China, Atmospheric chemistry and physics, 18, 7799–7814, https://doi.org/10.5194/acp-18-7799-2018, 2018.

Xu, H., Xiao, Z., Chen, K., Tang, M., Zheng, N., Li, P., et al.: Spatial and temporal distribution, chemical characteristics, and sources of ambient particulate matter in the Beijing-Tianjin-Hebei region, Science of The Total Environment, 658, 280–293, https://doi.org/10.1016/j.scitotenv.2018.12.164, 2019.

Yang, H.-H., Arafath, S., Lee, K.-T., Hsieh, Y.-S., and Han, Y.-T.: Chemical characteristics of filterable and condensable $PM_{2.5}$ emissions from industrial boilers with five different fuels, Fuel, 232, 415–422, https://doi.org/10.1016/j.fuel.2018.05.080, 2018.

Yang, Y., Liu, X., Qu, Y., Wang, J., An, J., Zhang, Y., and Zhang, F.: Formation mechanism of continuous extreme haze episodes in the megacity Beijing, China, in January 2013, Atmospheric Research, 155, 192–203, https://doi.org/10.1016/j.atmosres.2014.11.023, 2015.

Yang, Y., Wang, Y., Zhou, P., Yao, D., Ji, D., Sun, J., Wang, Y., Zhao, S., Huang, W., Yang, S., Chen, D., Gao, W., Liu, Z., Hu, B., Zhang, R., Zeng, L., Ge, M., Petäjä, T., Kerminen, V.-M., Kulmala, M., and Wang, Y.: Atmospheric reactivity and oxidation capacity during summer at a suburban site between Beijing and Tianjin, Atmospheric chemistry and physics, 20, 8181–8200, https://doi.org/10.5194/acp-20-8181-2020, 2020.

Yu, W., Ye, T., Zhang, Y., Xu, R., Lei, Y., Chen, Z., et al.: Global estimates of daily ambient fine particulate matter concentrations and unequal spatiotemporal distribution of population exposure: A machine learning modelling study, The Lancet. Planetary health, 7, e209–e218, https://doi.org/10.1016/S2542-5196(23)00008-6, 2023.

Zhang, H., Cheng, S., Yao, S., Wang, X., and Zhang, J.: Multiple perspectives for modeling regional $PM_{2.5}$ transport across cities in the Beijing–Tianjin–Hebei region during haze episodes, Atmospheric Environment, 212, 22–35, https://doi.org/10.1016/j.atmosenv.2019.05.031, 2019.

Zhang, J. K., Sun, Y., Liu, Z. R., Ji, D. S., Hu, B., Liu, Q., and Wang, Y. S.: Characterization of submicron aerosols during a month of serious pollution in Beijing, 2013, Atmospheric Chemistry and Physics, 14, 2887–2903, https://doi.org/10.5194/acp-14-2887-2014, 2014.

https://doi.org/10.5194/egusphere-2026-3211
Preprint. Discussion started: 5 August 2026

Zhang, S., Chen, S., Guo, B., Wang, H., and Lin, W.: Regional air-quality assessment that adjusts for meteorological confounding(in Chinese), Scientia Sinica(Mathematica), 50, 527–558, https://doi.org/10.1360/SCM-2019-0368, 2020.

Zhao, F., Wang, Y., and Xi, S.: Chemically Induced Decline in Wintertime SO2 Emission Control Efficacy, Environmental Science & Technology Letters, 12, 1190–1196, https://doi.org/10.1021/acs.estlett.5c00731, 2025.

Zhu, Y., Liang, Y., and Chen, S. X.: Assessing local emission for air pollution via data experiments, Atmospheric Environment, 252, 118 323, https://doi.org/10.1016/j.atmosenv.2021.118323, 2021.